Development of a piston cylinder calibrator

Document status and date:
Published: 01/01/2005

Document Version:
Publisher's PDF, also known as Version of Record (includes final page, issue and volume numbers)

Please check the document version of this publication:

• A submitted manuscript is the version of the article upon submission and before peer-review. There can be important differences between the submitted version and the official published version of record. People interested in the research are advised to contact the author for the final version of the publication, or visit the DOI to the publisher's website.
• The final author version and the galley proof are versions of the publication after peer review.
• The final published version features the final layout of the paper including the volume, issue and page numbers.

Link to publication

Download date: 16. Nov. 2023

Development of a piston cylinder calibrator

T. de Boer

DCT 2005.106

DCT traineeship report

Supervisors:
Dr. J. Miles
P. Cox, BSc
Prof. Dr. Ir. M. Steinbuch

National Measurement Institute (NMI)
Clayton Laboratory
Victoria, Australia

Technische Universiteit Eindhoven
Department of Mechanical Engineering
Dynamics and Control Technology Group

Eindhoven, July 2005

Contents

Chapter 1

Introduction

1.1 Diameter and form measurement of cylinders

At the National Measurement Institute (NMI) in Melbourne, an instrument is currently developed capable of measuring the diameter and form of cylinders. The main impetus for the development of the instrument is a requirement by the NMI pressure group to accurately characterize the geometry of cylindrical pistons used in pressure standard devices. Hence the name: Piston Cylinder Calibrator. The need is to measure the diameter, roundness and straightness of cylinders ranging in diameter from 2 to 30 mm with an uncertainty of plus or minus 10 nanometers. [9]

1.2 Problem definition an objective

The instrument is constructed with help of the National Research Counsel in Ottawa, Canada. The parts are shipped to Melbourne and recently put together in the dimensional laboratory of the NMI. Problem is that the capabilities of the new instrument are not known. Goal of this project is to investigate uncertainties in the measurement process. Furthermore LabVIEW software should be written to replace existing software.

1.3 Overview

Background information about the project and a description of the Piston Cylinder Calibrator is given in Chapter 2. Chapter 3 describes reducing errors by tuning a controller for two DC motors which are part of the instrument. Errors in the measurement caused by two interferometers are discussed in Chapter 4. Chapter 5 describes a few important experiments performed with the instrument. The results are discussed in Chapter 6 and recommendations are done for future research on the instrument. Finally conclusions of this research project are given in Chapter 7.

This study has been conducted as a three month student internship for the faculty of Mechanical Engineering at the University of Technology Eindhoven.

I would like to thank all the employees of the NMI Clayton laboratory and especially my supervisors: Dr. John Miles and Peter Cox, BSc.
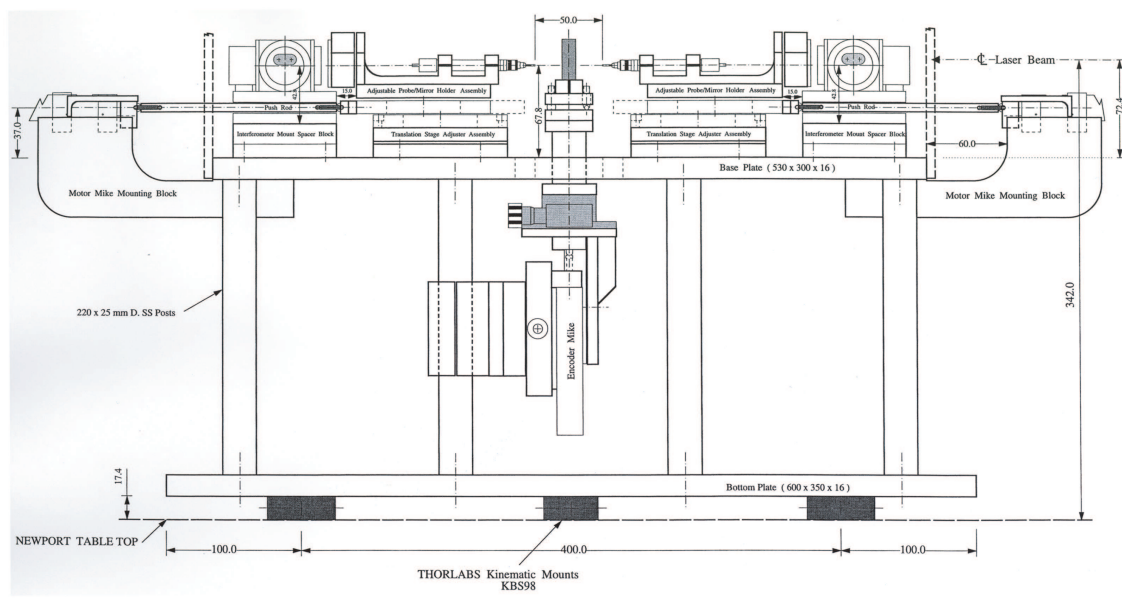
Figure 1.1: CAD drawing of the instrument, side view
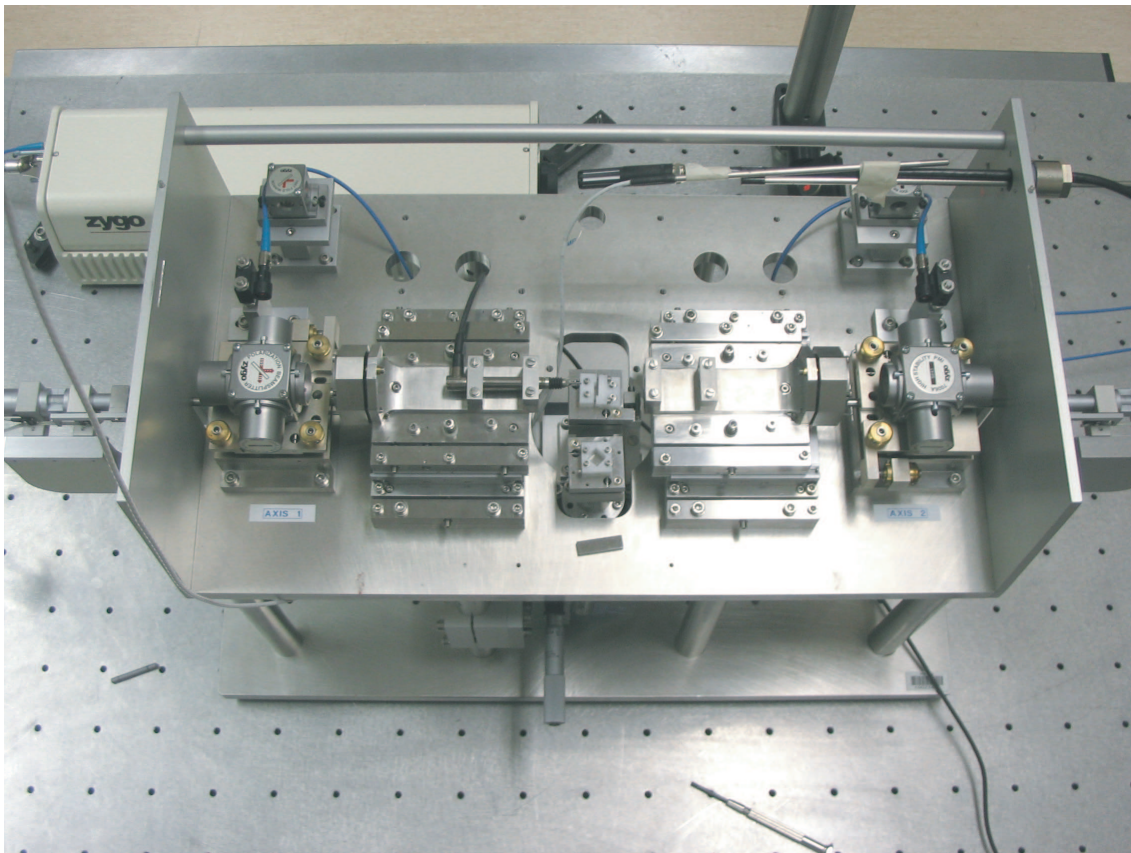
Figure 1.2: Photo of the instrument, top view

Chapter 2

Description PCC instrument

2.1 Pressure standards

High pressure standards (of up to 250 MPa) are commonly realized using piston gauges, consisting of accurately machined and close fitting pistons and cylinders. Weight is added to the vertically positioned cylinder which will generate a pressure in the fluid inside the vessel.The pressure generated in the fluid is given by [9].

$$p_{fluid} = \frac{Mg}{A} \qquad (2.1)$$

Where M is the total effective mass of the piston and A the effective area. Uncertainties required
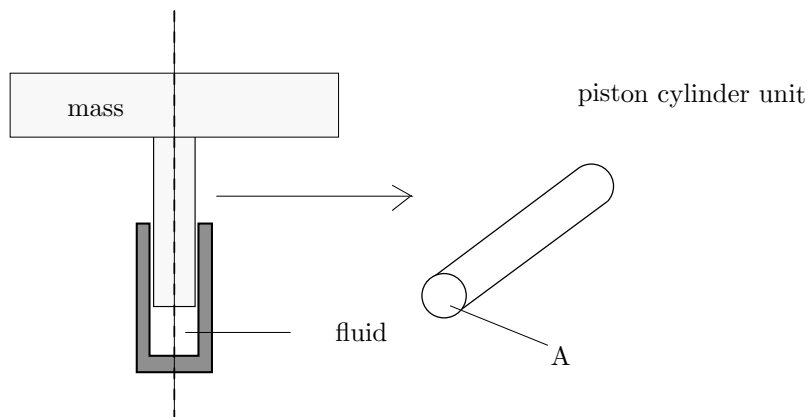
Figure 2.1: Schematic representation high pressure standard

for the realization of pressure using piston gauges are typically below 10 ppm. It follows that the area A of the piston cylinder unit (PCU) should be calculated better than 10 ppm. This requires that the diameter, roundness and straightness of these pistons should be measured with uncertainties below 5 ppm. Typical cylinder diameters range from 2 to 30 mm implying that the diameter and form of these pistons needs to be measured with uncertainties of plus or minus 10nm. These requirements are currently beyond NMI's capabilities and the developed Piston Cylinder Calibrator (PCC) should therefore provide this capability.

2.2   Description instrument

The PCC instrument is located in the Dimensional lab of the NMI as shown in figure 1.2. A CAD drawing of the instrument is shown, figure 1.1. The parts most relevant to this research will briefly be described in this section.

2.2.1   Basic setup

The instruments structure is entirely made of stainless steel. The baseplate is mounted statically determined onto an air suspended table using kinematic mounts. Eight posts support the top plate. Two of these posts also support a vertical spindle mechanism that clamps a piston cylinder unit and enables rotation and translation of the PCU.
Two mutually opposed LVDT probes are used to make contact with the surface of the cylinder. Together with a plain mirror these probes are mounted onto a high precision stage with magnetic kinematic bearings. These stages are capable of translating towards and away from the PCU with a maximum stroke of 25 mm. Two DC motors (see Chapter 3 for more information) are used to translate the stages via a push rod. The movement of the stages is measured using a ZYGO ZMI 2000 heterodyne laser (see Chapter 4 for more information). The laser is mounted next to the instrument, the laser beam enters the construction on the back and a beamsplitter splits the beam into two beams. One of the beams will directly enter a high stability plain mirror interferometer assembly. This interferometer is part of the axis called axis 2. The other beam enters a second interferometer, (part of axis 1) via a beam bender. The whole top plate can be covered using a transparent polystyrene or stainless steel cover.

Method of measurement

No PCU measurements are yet performed on the instrument. The desired method of measurement is briefly described here. The two stages are translated till the two contact probes make contact. At this starting point the readout of the laser and probes is logged. The stages retract and allow a PCU to be placed on the vertical axis. The stages are translated back towards the PCU and will keep moving as the probes make contact with the PCU. The readout of the probes will, at some point, be identical to the logged value at the start. The total displacement of both stages (monitored by the interferometers) relative to their start position is, at this position, equal to the diameter of the PCU.

2.2.2   Other equipment

Next to the PCC setup a rack contains all equipment relevant to conducting measurements on the PCC setup. It contains a:

- PC running on Windows 98, 366 MHz Intel Pentium processor, 128 kb RAM, supplied with:
    NI LabVIEW software [5]

    ZYGO ZMI measurement software

    QMove software to control DC motors

- VAISALA humidity sensor

- SETRA pressure sensor

- ZYGO ZMI 2001 measurement board

- a HP 3488A scanner

2.2.3 Working with the PCC

After connecting all the equipment and aligning the stages to the measurement laser beam, a quick experiment is performed to get more insight in the behavior and accuracy of the PCC system. Both plane mirrors are removed and a reflecting steel cube is fixed onto the first stage. Both measurement beams reflect on the cube and measure it's position change. A macro of command lines in Qmove is used to translate the first stage a few times. The ZMI software monitors the position change as can be seen in figure 2.3. Some inexplicable behavior was witnessed if we zoom in on these results. Looking at figure 2.4 we can conclude that :

- a drift away from the zero position is monitored after starting the measurement

- the desired displacement of 1500 μm isn't measured

- both interferometers don't measure the same relative displacement

- when the motor stops moving, movement of the cube is still measured

- the cube is not returning to it's initial position

To find out what causes these errors, research is performed to get insight in the behavior of the DC motors (Chapter 3), the laser setup (Chapter 4) and the mechanical structure (Section 5.4).
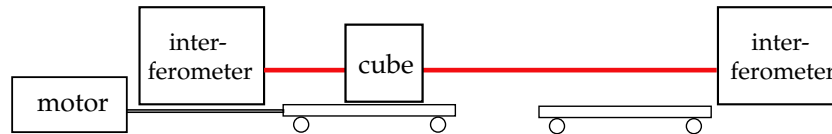
Figure 2.2: Schematic representation experimental setup
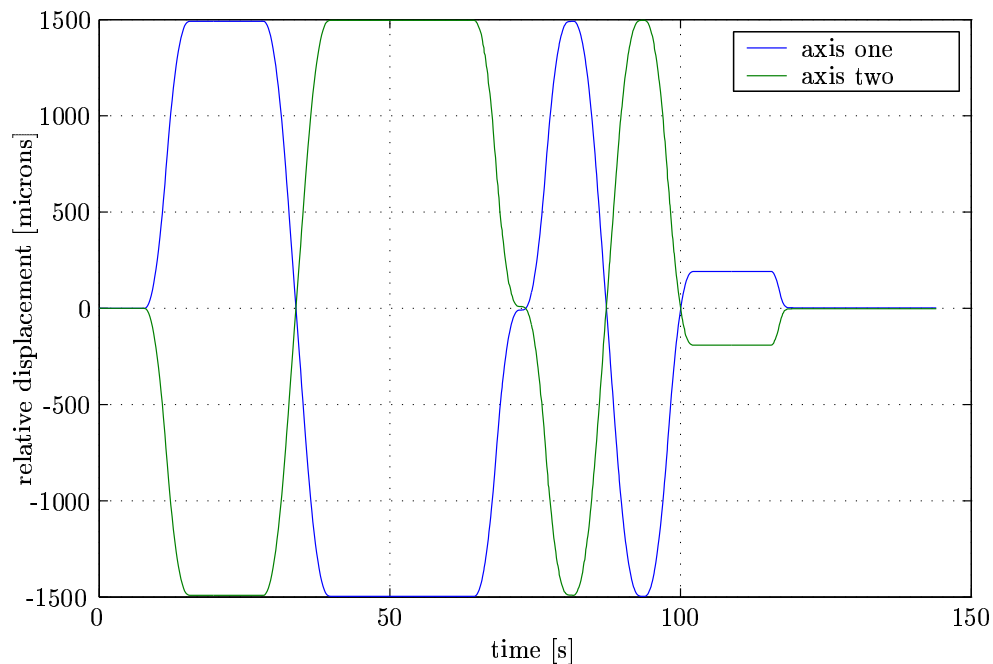
Figure 2.3: Relative motion of left stage. Movement positive for axis one when moving from axis one to two.
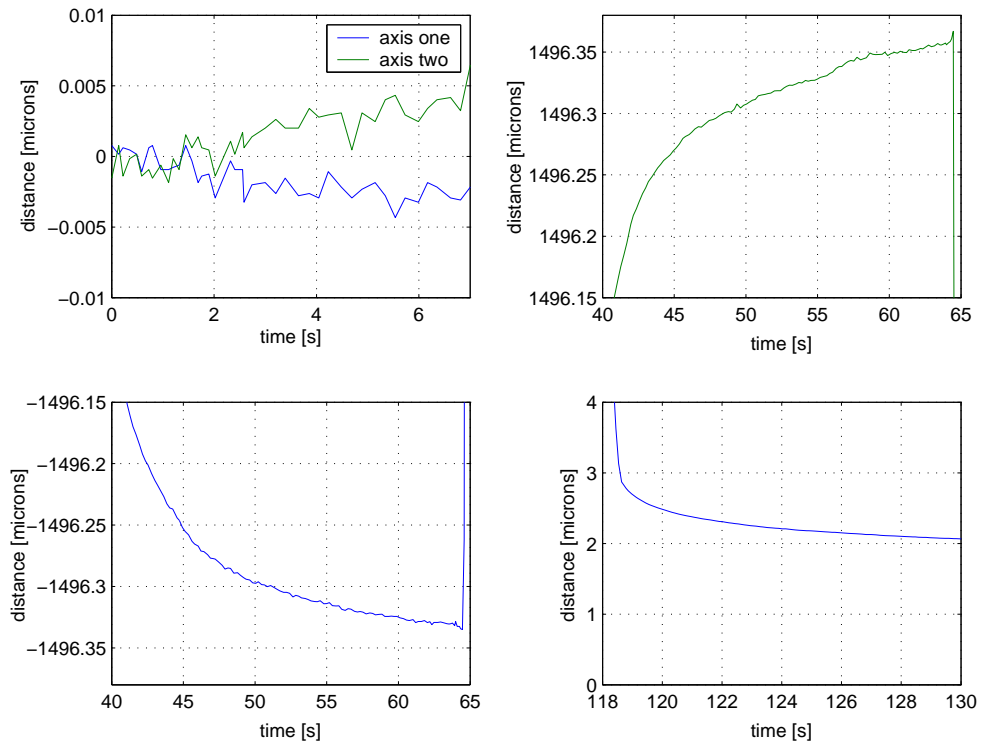
Figure 2.4: Several zoom boxes of motion shown in figure 2.3

Chapter 3

DC Motors

The two motors used to translate the stages are two identical Physik Instrumente (PI) M-224.2 High Resolution DC-Mike actuators. They consist of a micrometer drive with non-rotating tip driven by a closed loop DC motor-gearhead combination with motor shaft mounted encoder. Their travel range is 25 mm and bounded by two electrical limit switches. The encoder has a resolution of 60 counts/rev, combined with a gear ratio of $\left(\frac{31}{9}\right)^4 : 1$ and a pitch of 0.5 mm/rev the resolution of the motor is about 60 nm. Both motors are controlled using a PI C-842 motor controller board which is installed in a 16 bit ISA PC slot. Motion and PID control parameters can be altered through the supplied Windows software QMove which uses easy command lines. Unfortunately no tracking or position errors can be analyzed using QMove.

More information is needed about the control capabilities of the chipset and the system itself to control the system in an appropriate way.

3.1   Chipset

The C-842 controller is supplied with two PMD MC1201A motion chips [1]. It consists of two 68 pin PLCC's both fabricated in CMOS. The Peripheral Input/Output IC (I/O chip) is responsible for interfacing to the host processor and to the position input encoders. The Command Processor IC (CP chip) is responsible for all host command, profile and servo computations, as well as for outputting the DC signals. The encoder signals are input to the I/O chip in quadrature format. With use of hexadecimal commands, communication with the chipset is possible which allows profile and control parameters to be changed. Low level LabVIEW VI's (virtual instruments) are supplied to send hexadecimal commands lines. The control parameters that can be changed are:

- proportional gain

- derivative gain

- integral gain

- integration and motor output limit

The relevant profile parameters that can be changed are:

- set to S-curve profile

- set to trapezoidal profile

- set to velocity-contouring profile

- set to electronic gear

- desired position

- maximum velocity

- maximum acceleration

3.2   System identification

3.2.1   FRF measurement

To gain more insight in the dynamic behavior of the system a frequency response function measurement is desired. The system can be operated is open loop mode and therefore a frequency response function (FRF) can be determined using auto- and cross powerspectra. The measured cross powerspectrum is divided by the measured auto powerspectrum to create an estimator for the frequency response function. Therefore the systemresponse at a known input should be measured. White noise superimposed on a sine wave as a reference trajectory is a good choice: white noise contains all frequencies and the sine wave will make sure the system performs an overall smooth motion (no stalling or cogging). This FRF measurement would require measurement of a reference signal and the encoder position signal in time. LabVIEW will be used to perform the measurement. In the subsequent paragraphes the preparations needed to perform this FRF measurement are described.

White noise generator

A DAC card is installed on the computer and a LabVIEW VI is written to generate a DC voltage to empower the motor. Unfortunately LabVIEW was not able to generate a sine wave with superimposed white noise in real-time mode. Writing the generated signal data to a buffer proved to be successful: operating the motor with use of the DAC card is now possible.

Encoder signal

The controller board is needed to read the encoder counts: it interprets the quadrature data signal coming from the encoder. Using hex code 37 in a LabVIEW VI the encoder count can be read from the controller card. Though the controller board of the motors is capable of reading both axes at 10 kHz, sampling the encoder signal at a high rate proves to be difficult. At first a maximum sample rate of 20 Hz is achieved. Furthermore it seems that the sample rate is not constant. Measurements show that the sample rate of LabVIEW changes and is strongly influenced by other processes active on the computer. Even movement of he mouse of the computer strongly influences the maximum sample rate. By reprogramming the VI to minimize the calculation time of the VI itself and shutting down several programs on the computer a maximum sample rate of about 170 Hz was achieved.

Problems

The VI to read the encoder signal and the VI to generate an input signal are combined. Logging both signals together with a time stamp is sufficient to perform a FRF measurement.
Unfortunately it was found that a variable delay of about 3 seconds was present between LabVIEW and the actual output of the DAC card. Therefore the logged LabVIEW signal did not match the true output signal of the DAC card. Furthermore it was found that the computer (or LabVIEW) was not capable of communicating with the DAC card and the controller board at the same time. It resulted in a sample rate of the encoder signal of about 1 Hz. With the available equipment it proved to be too hard to perform a FRF measurement in order to find a suitable controller. Therefore the system is inspected in the time domain, which is explained in the next paragraph.

3.2.2 Time domain

A transient dynamic response, such as comes from a step or impulse, can be used to obtain a dynamic model of the system. The controller board is unfortunately not capable of generating a step or impulse input. It is however capable of generating a trapezoidal profile, where the acceleration and velocity are bounded. Therefore it is decided to tune the controller looking at the dynamic response on this reference profile.
Characteristic properties of a step respons are illustrated in figure 3.1 and will also be used to characterize a trapezoidal response. The rise time r_t is defined as the time it takes to reach the
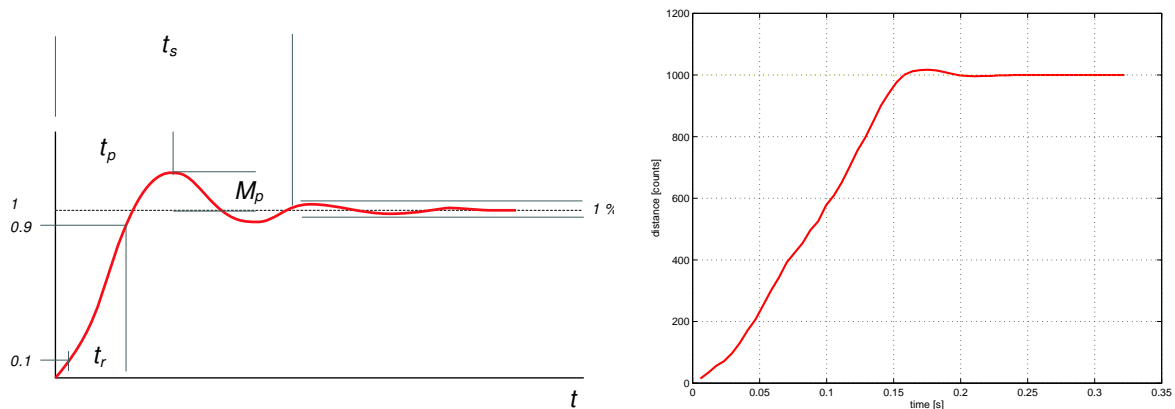
Figure 3.1: Left: characteristics step response. Right: example of system response on trapezoidal reference trajectory $(P = 300, I = 0, D = 750)$.

vicinity of the set point. (The speed of the motors during the rise time is equal in all situations and bounded to 414 μm/s.) The settling time t_s is the time it takes the system transients to decay. The overshoot M_p is the maximum amount of the system overshoots its final value divided by its final value. The peak time t_p is the time it takes the system to reach the maximum overshoot point [8].
It must be noted that very accurate comparisons between all data can't be made since the sample rate changes slightly during logging, which can be seen in figure 3.1(right side).
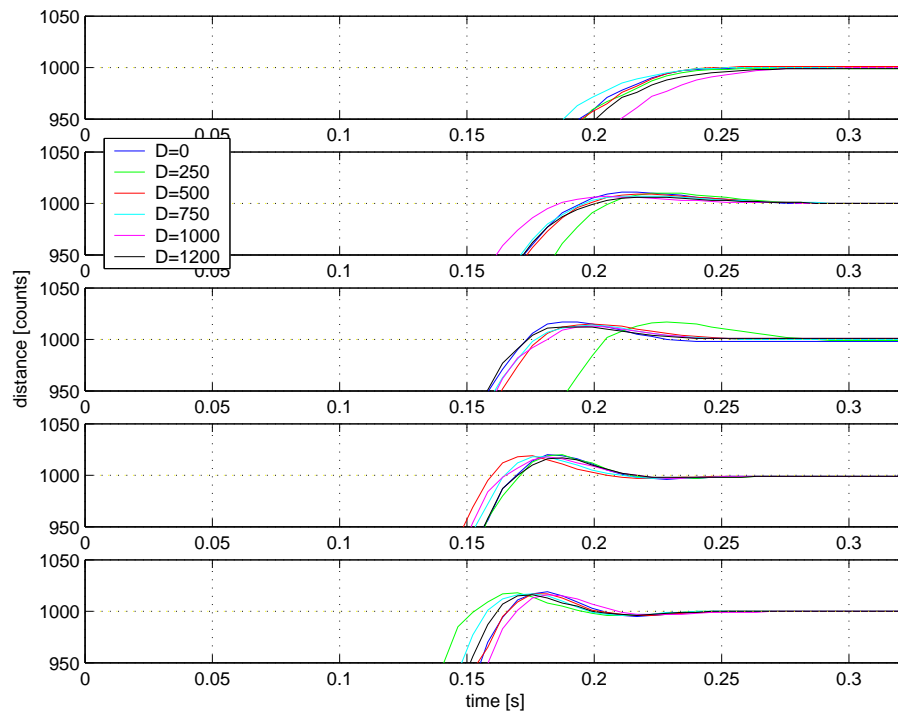
Figure 3.2: System response for different values of P and D. I is zero. From top till bottom: P=100;150;200;300;400. Graphs show response near setpoint.
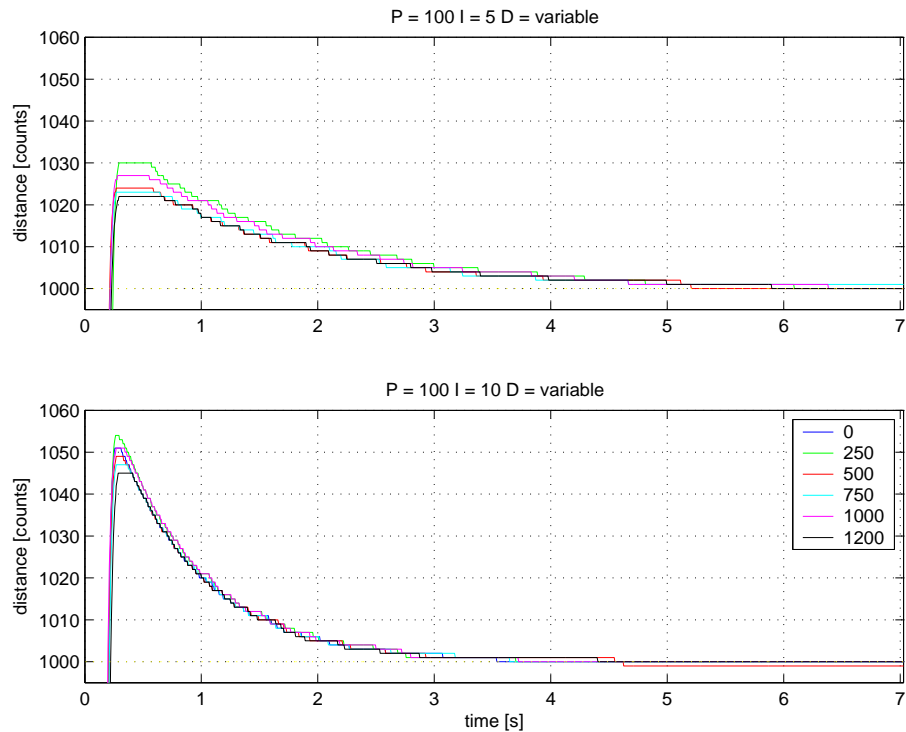
Figure 3.3: System response for different values of D and I. $P = 100$.

For different control parameters the time response of the system is compared, as can be seen in figure 3.2. The software allows a maximum proportional, integral and derivative gain of 400, 10 respectively 1200. (The specific PID control algorithm could not be found in literature). Increasing the proportional gain leads to an expected increasing overshoot and decreasing settling time. Changing the derivative gain doesn't change the respons significantly. A steady state error is present in almost all cases. Since accuracy is very important in the present setup an integral action is added. For $P = 100$ the response is shown in figure 3.3. The integral action unfortunately increases the settling time but does eliminates the unwanted steady state errors. Increasing the integral gain leads to an increasing overshoot, but decreases the settling time. A high integral action, $I = 10$, is in this case preferred. Furthermore it can be seen that a high derivative action does have an effect on the overshoot: increasing D leads to a decreasing overshoot. So $D = 1200$ seems a good choice. From figure 3.4 it can be seen that, with $I = 10$ and $D = 1200$ a high proportional gain of 400 is preferable since it decreases the overshoot and settling time even further.
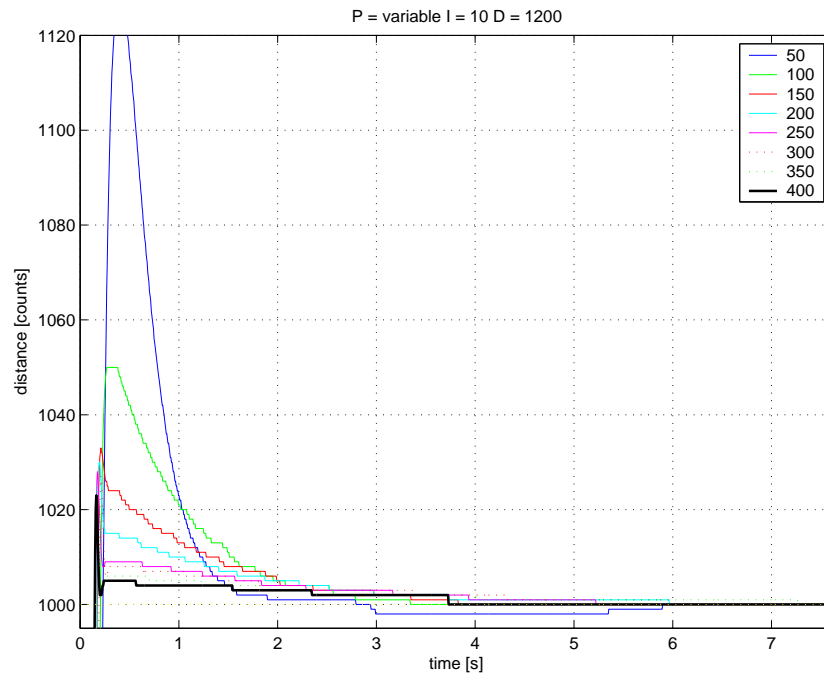
Figure 3.4: System response for different values of P. $I = 10$ and $D = 1200$.

3.3   Stages

With a suitable controller it is now possible to accurately control the motor (or encoder) position. This however does not mean it is possible to control the position of the stage accurately. But the measuring method doesn't require this, so this is not a problem. It only requires the position change to be accurately monitored, which will be done by the laser.

To gain a bit more insight in the behavior of the stage relative to the motor some experiments were however conducted. The system was translated up and down several times while the position changes were monitored by the laser. They revealed a backlash in the motor gears of about 5 μ m (in accordance with specifications manufacturer) and a large settling time of the stage after coming to a halt. It takes the stage about a minute to come to an equilibrium as can be seen in figure 3.5.

Figure 3.5: Measured movement of the stage

Chapter 4

Interferometry

As mentioned in Chapter 2 inexplicable behavior was witnessed during a first measurement. In the previous chapter attention has been given to the minimization of the position error of the DC motors used. Now, the uncertainties caused by the interferometer will be investigated. First, the working principle of the interferometers is briefly explained.

4.1   HeNe Laser

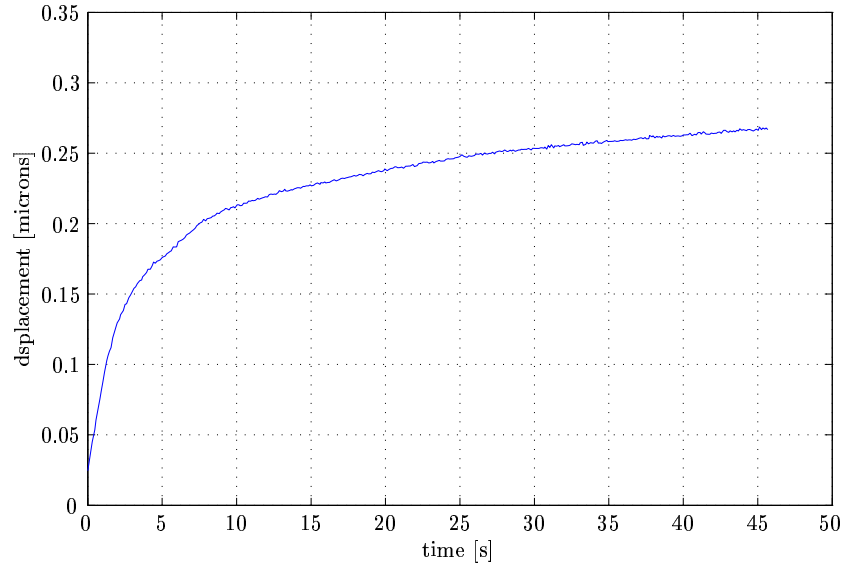The source for a heterodyne interferometer system is a Helium Neon laser whose outputs contains two slightly different, orthogonally polarized, frequencies. A polarizing beam splitter is used to separate both light components, making light of frequency f_1 travel a measurement path, while light of frequency f_2 travels a reference path. For two beams of light to interfere, the beams must have the same polarization state. The beams are therefore recombined and polarized at a receiver and a optical interference signal can be monitored. If the movable target remains stationary, the frequency of the optical interference signal (the beat frequency) will be the exact difference between the lasers at two frequencies ($f_2 - f_1$). When the target moves, the frequency of the optical interference signal will be shifted up or down by the Doppler effect depending on the direction of motion ($f_2 - (f_1 \pm \Delta f_1)$). Heterodyne detection makes a phase comparison between a measurement beat signal of unknown frequency to a reference beat signal of known frequency at discrete time intervals. The phase difference between the two signals is measured and any phase changes are digitally accumulated, representing a change in optical path length. The measurement data can be read in the form of an 8, 16 or 32 bit 2's complement word.

4.2   Airflow

To eliminate all errors caused by nonlinearities in the movement of the stage or motor, or misalignments in the interferometric setup, neither the stage nor the gauge cube will be moved during the measurement. The gauge cube has two reflective sides which means that the laser signal of both axis can be used to monitor it's position (same as situation shown in figure 2.2. At the start of the measurement the position is set to zero and the drift in the position signal during time is monitored. It was found that a much smoother position signal was measured if the cover was placed onto the top steel plate, as can be seen in figure 4.2.
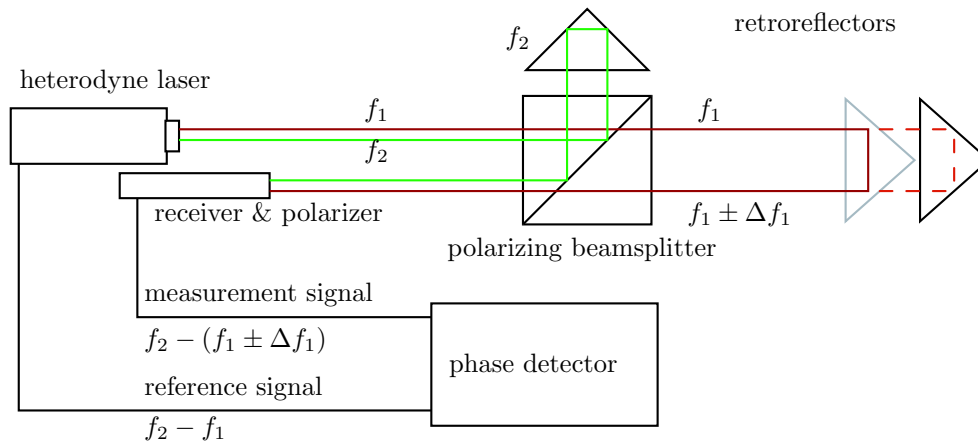
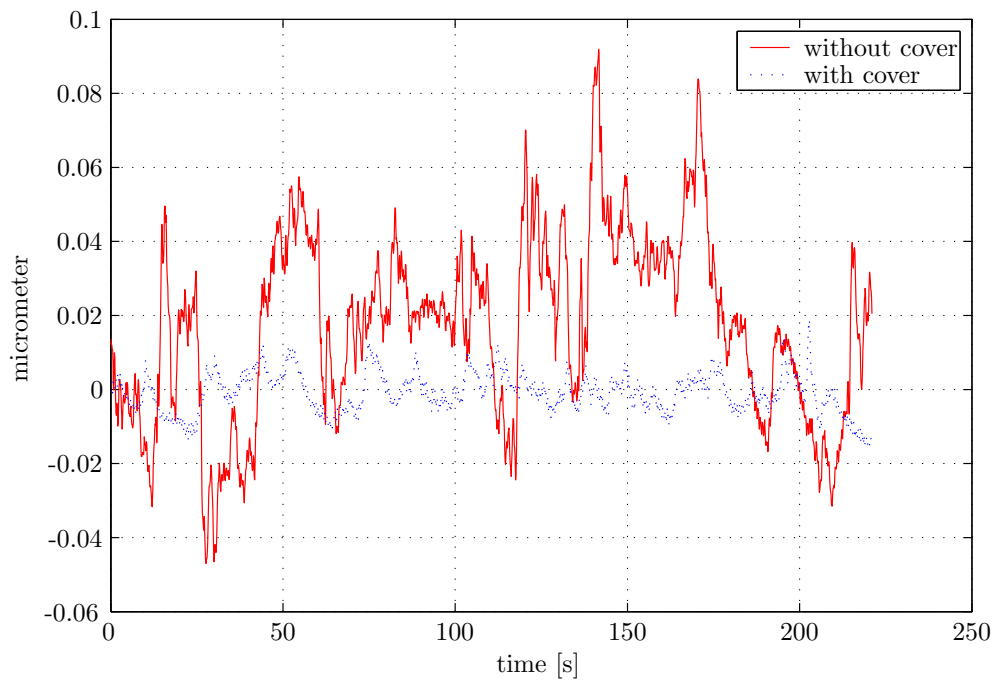Figure 4.1: Single pass interferometer

Figure 4.2: The drift away from the zero position measured in two cases, with and without cover.

These measurements were taken at a different times and therefore different environmental conditions. It can however be seen that the cover smoothens the position measurement considerably by preventing inhomogeneous airmixtures to flow through the laserpath. The cover can however not prevent a drift away from the initial zero point. The drift measured at axis two, which's measurement path was twice the distance of axis one, was much larger compared to axis one. Therefore it was very likely that the drift was caused by changes in the refractive index of air. The influence of this change is therefore examined.

4.3 Change in refractive index

The displacement measured with an interferometer depends on the wavelength of the light used. The wavelength depends on the refractivity of the medium through which it passes according to the relationship

$$\lambda = \frac{\lambda_{vac}}{n} \tag{4.1}$$

where λ_{vac} is the wavelength in vacuum and n is the refractive index of the medium. Changes in the environment affect the refractive index, thus altering the required compensation to the interferometric measurement. Accurate knowledge of the refractivity is therefore needed to perform precise length interferometry. In literature, several equations can be found to calculate the correction for the effect of the refractive index of air on the vacuum wavelengths of light. They are are based on empirical equations which use physical parameters of the air such as air pressure, relative humidity and air temperature and CO_2 content. Three of these equations are compared in [7] and based on these findings, the Ciddor equations are used to calculate the refractive index of air.

4.3.1 Ciddor equations

The Ciddor equations are briefly described [4] [7]. Input parameters in the Ciddor equations are vacuum wavelength λ_{vac} in μm, temperature t in °C, pressure p in in Pa, relative humidity RH in % and CO_2 content in ppm. The refractivity $(n-1)$ of air is calculated by assuming that the refractivity of each air component can be added to other components. Therefore the refractivity of dry air $(n_{axs} - 1)$ multiplied by its density $\rho_a xs$ relative to the dry air component of moist air ρ_a can be added to the product of the refractivity of pure water vapor $(n_{ws} - 1)$ and its density $\rho_w s$ relative to the water vapor component of moist air ρ_w.

$$n_{prop} - 1 = \left(\frac{\rho_a}{\rho_{axs}}\right)(n_{axs} - 1) + \left(\frac{\rho_w}{\rho_{ws}}\right)(n_{ws} - 1). \tag{4.2}$$

Now each of these terms has to be evaluated. The refractivity of dry air is given by:

$$(n_{axs} - 1) = (n_{as} - 1)\left(1 + 0.534 \cdot 10^{-6}\,(x_c - 450)\right) \tag{4.3}$$

Where $(n_{as} - 1)$ is the refractivity of standard dry air (with a CO_2 content of 450 ppm) given by

$$10^8\,(n_{as} - 1) = \frac{k_1}{(k_0 - \sigma^2)} + \frac{k_3}{(k_2 - \sigma^2)} \tag{4.4}$$

$k_0 = 238.0185 \ \mu m^{-2}$
$k_1 = 5792105 \ \mu m^{-2}$
$k_2 = 57.362 \ \mu m^{-2}$
$k_3 = 167917 \ \mu m^{-2}$

where σ is the wave number (reciprocal of the vacuum wavelength). For the refractivity of pure water vapor the following equation holds

$$10^8 \left(n_{ws} - 1\right) = 1.022 \left(w_0 + w_1\sigma^2 + w_2\sigma^4 + w_3\sigma^6\right) \tag{4.5}$$

$w_0 = 295.235 \ \mu m^{-2}$
$w_1 = 2.6422 \ \mu m^{-2}$
$w_2 = -0.032380 \ \mu m^{-4}$
$w_3 = 0.004028 \ \mu m^{-6}$.

The densities ρ_i can all be derived using the general expression

$$\rho = \frac{pM_a}{ZRT}\left(1 - x_w\left(1 - \frac{M_w}{M_a}\right)\right) \tag{4.6}$$

M_a = molar mass of dry air in kg/mol, see (4.7)
M_w = molar mass of water vapor, 0.018015 kg/mol
T = temperature in degrees Kelvin
R = revised molar gas constant, 8.314510 Jmol^{-1}K^{-1}
Z = compressibility factor of moist air, see (4.8)
x_w = molar fraction of water vapor in moist air , see (4.9)

where M_a is given by

$$M_a = 10^{-3}\left(28.9635 + 12.011\dot{1}0^{-6}\left(x_c - 400\right)\right) \tag{4.7}$$

and the compressibility factor of moist air

$$Z = 1 - \left(\frac{p}{T}\right)\left(a_0 + a_1t + \left(b_0 + b_1t\right)x_w + \left(c_0 + c_1t\right)x_w^2\right) + \left(\frac{p}{T}\right)^2\left(d + ex_w^2\right) \tag{4.8}$$

a_0 = $1.58123 \cdot 10^{-6}$ K Pa^{-1} c_0 = $1.9898 \cdot 10^{-4}$ K Pa^{-1}
a_1 = $-2.9331 \cdot 10^{-8}$ Pa^{-1} c_1 = $-2.376 \cdot 10^{-6}$ Pa^{-1}
a_2 = $1.1043 \cdot 10^{-10}$ K^{-1} Pa^{-1} d = $1.83 \cdot 10^{-11}$ K^2 Pa^{-2}
b_0 = $5.707 \cdot 10^{-6}$ K Pa^{-1} e = $-0.765 \cdot 10^{-8}$ K^2 Pa^{-2}
b_1 = $-2.051 \cdot 10^{-8}$ Pa^{-1}

and x_w given by

$$x_w = \frac{fhp_{svp}}{p} \tag{4.9}$$

with f being the enhancement factor of water vapor in air, h the fractional humidity and p_{svp} the saturation vapor pressure of water, given by:

$$f = \alpha + \beta p + \gamma t^2 \tag{4.10}$$

$$h = \frac{RH}{100} \tag{4.11}$$

$$p_{svp} = e^{AT^2 + BT + C + DT^{-1}}. \tag{4.12}$$

A = $1.2378847 \cdot 10^{-5}$K^{-2} α = 1.00062
B = $-1.9121316 \cdot 10^{-2}$K^{-1} β = $3.14 \cdot 10^{-8}$Pa^{-1}
C = 33.93711047 γ = $5.6 \cdot 10^{-7}$°C^{-2}
D = $-6.3431645 \cdot 10^3$K

Sensitivity

For a better understanding of the Ciddor equation, the influence of the different parameters temperature, pressure and humidity is evaluated. The Ciddor equations consists of many complex equations. Therefore the sensitivity is investigated by determining the refractive index for different input values (instead of an analytical way). A range of values was chosen in accordance with
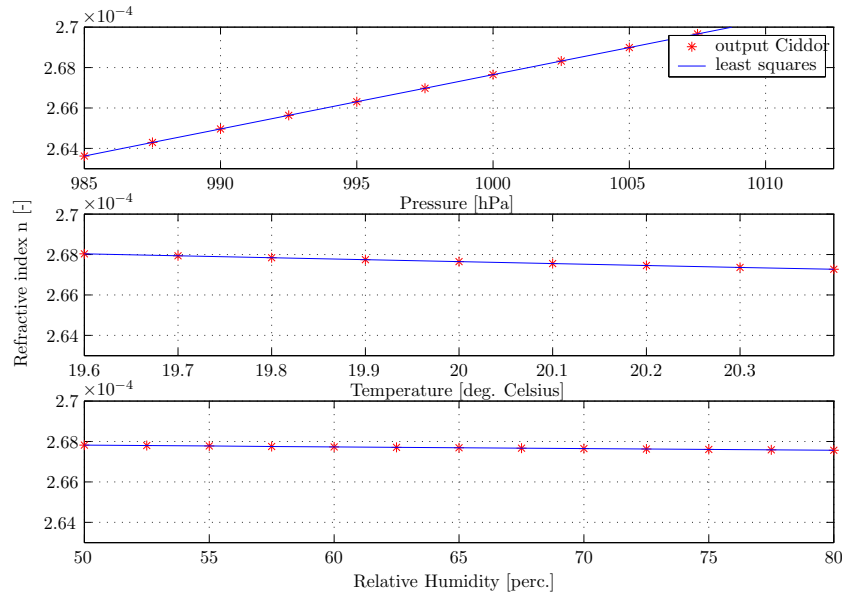
Figure 4.3: Independently, an offset is given to three input parameters for λ=632.991528nm. Common situation p=1000 hPa, T=20°C and 70%RH for which n_{prop}=1.000267648.

expected daily changes in the laboratory environment. As we can see in figure 4.3 all the relations are virtually lineair within that specific range. The following sensitivities were found:

$$\frac{\delta n}{\delta p} = 2.68 \cdot 10^{-7} hPa^{-1} \tag{4.13}$$

$$\frac{\delta n}{\delta T} = -9.53 \cdot 10^{-7} K^{-1} \tag{4.14}$$

$$\frac{\delta n}{\delta RH} = -8.48 \cdot 10^{-9} \%RH^{-1} \tag{4.15}$$

$$\frac{\delta n}{\delta CO_2} = 1.44 \cdot 10^{-10} ppm^{-1} \tag{4.16}$$

$$\tag{4.17}$$

It must be noted that these sensitivities were found using the least squares method on a relatively small number of data points (10). However, the found sensitivities agree in an acceptable way with values found in literature [6].

These sensitivities imply that in an interferometric measurement, a +1 ppm error would occur if the environmental conditions would change in one of the following ways:

- a $+0.100 \cdot 10^{-5}$ change in the refractive index of air, which means a:

- a +3.7 hPa change in air pressure

- a -1.1°C change in air temperature

- a +120 % change in the relative humidity of air

- a +7000 ppm change in the CO_2 content of air

It may be concluded that for daily use in metrology laboratories the pressure measurement is most important, followed by temperature, humidity and carbon dioxide content. Which is also illustrated in figure 4.3.
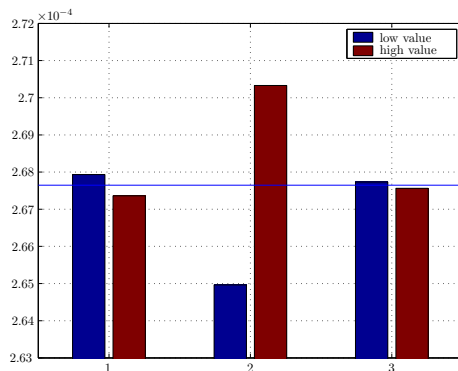

Figure 4.4: Barplot for two values in of the three input parameters. For λ=632.991528nm. Horizontal line indicates common situation p=1000 hPa, T=20($^\circ$)C and 70%RH. (Daily variation of 100 ppm CO_2 content not shown.) Bar 1: Temperature 19.7 and 20.3°C. Bar 2: Pressure 990 and 1010 hPa. Bar 3: Relative humidity 60 and 80 %

4.3.2 Compensation for refractive index change

By measuring pressure, temperature and relative humidity of air, an accurate compensation can be performed using equation 4.1 for a changing laser wavelength. However, change in refractivity also affects the measurement in another way. The physical location of the starting or zero point of an interferometric measurement is monitored by the optical path rather than the physical path. At the zero point there is a difference in optical path between the measurement beam and the reference beam. Therefore environmental changes cause the accumulated fringes to change even when the physical displacement of the target mirror is zero.

In the ideal case the zero point is equal to the physical zero point, where there is no optical pathlength difference between reference and measurement beam. Since this is not possible, this difference in optical path, so called deadpath, should be compensated for.

The total deadpath distance consists of a fixed deadpath in the interferometer (caused by a difference between reference path distance R and measurement path M) and a variable dead path D depending on the zero point location (see figure 4.5). The total deadpath distance L_d is therefore given as [13]:

$$L_d = (M - R) + D \tag{4.18}$$

For the high stability plain mirror used in the setup, M is 14.22 mm and R is 13.08 mm. [1]

4.3.3 Compensation algorithm

The optical path change of the ZMI 2000 is given by [13] [11]

$$OPC = \frac{C\lambda_v}{512}, \tag{4.19}$$

---

[1]The high stability plain mirror used, is designed that both reference beam and measurement beam pass through equal amounts of glass. Thermal changes will therefore not influence the total deadpath length.
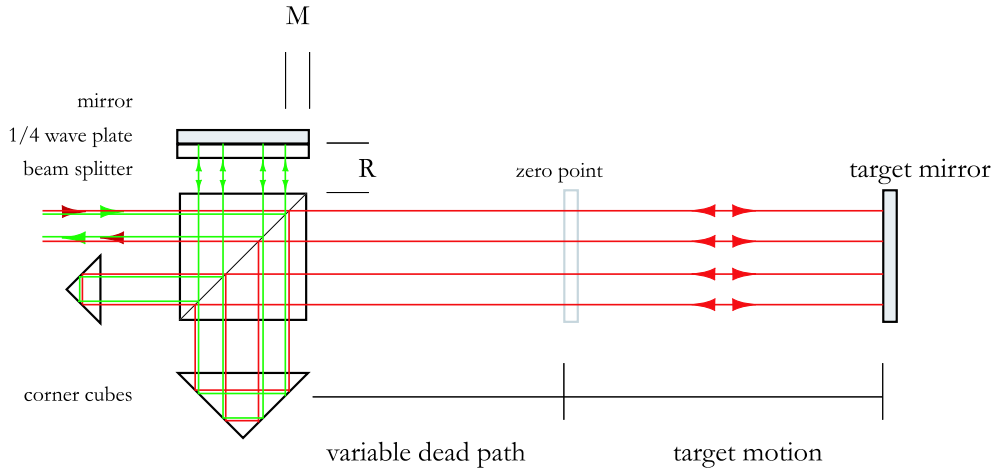
Figure 4.5: Representation of a four pass high stability plain mirror interferometer. Red line being the measurement beam, the green being the reference beam.

where C is the number of counts that pass trough the interferometer.

To increase the resolution, a four pass interferometer is being used which means a linear displacement of the target mirror l will result in an optical path change equal to $8l$. The true physical displacement of the target mirror is therefore given by

$$L = \frac{C\lambda_v}{n4096}.$$ (4.20)

The target motion relative to the zero point is the length we are interested in. Using equation (4.20) this motion is given by [12] , [3]:

$$L_m = (C_{acc} + C_{L_d}) \frac{\lambda_v}{n\left(t\right)4096} - L_d.$$ (4.21)

Where C_{acc} are the accumulated counts measured, and C_{L_d} is the total deadpath distance in terms of counts at time $t = 0$. Using equation (4.20) it follows that

$$C_{L_d} = \frac{L_d}{\frac{\lambda_v}{n(0)4096}}.$$ (4.22)

Combining equations (4.22) and (4.21) result in the following deadpath compensation algorithm

$$L_m = C_{acc} \frac{\lambda_v}{n(t)4096} + L_d \left(\frac{n(0)}{n(t)} - 1\right).$$ (4.23)

This algorithm will be used in the measurement software written in LabVIEW. Information about all the written LabVIEW software can be found in Appendix A

Chapter 5

Experiments

5.1 Introduction

The written LabVIEW software is used to do an experiments to see if the compensation algorithm 4.23 works. The results of this experiment have lead to several other experiments. All experiments are closely related to each other and are therefore described and analyzed in this chapter. A brief summary of all the results can be found in paragraph 5.7.

5.2 Correcting for changes refractivity of air

5.2.1 Description experiment

Goal of the experiment is to find out if the algorithm will eliminate the drift away from the zero position. The top cover is placed on the PCC and the plain mirrors are mounted back onto the stages. LabVIEW logs the accumulated counts of axis one, air pressure, relative humidity, temperature and the calculated refractivity at a sample rate of 1 Hz during a period of 15 hours. The total dead path length was chosen as large as possible, being 36 mm, to monitor the largest drift possible. The setup is shown in figure 5.1.
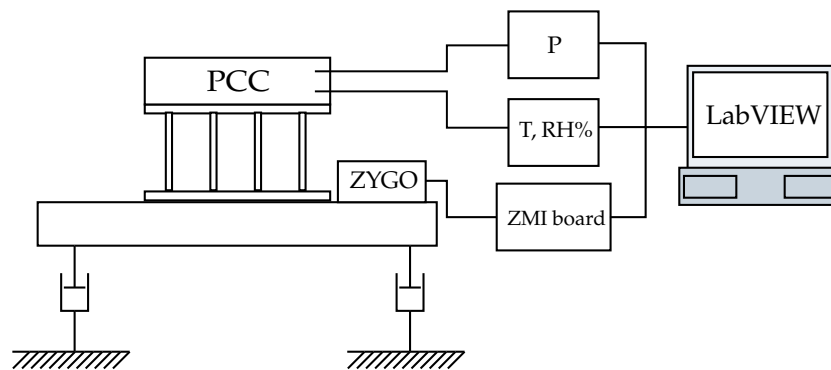

Figure 5.1: Drawing of the setup with the PCC and ZYGO laser mounted on an air suspended table. The three sensors and ZMI board are connected to the computer.
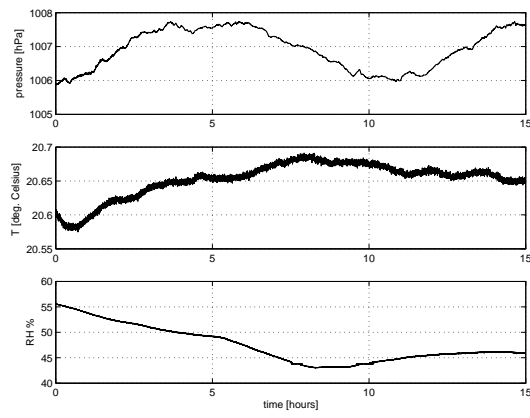
Figure 5.2: Environmental changes during time

Figure 5.3: Accumulated counts, converted to nanometers, measured with laser
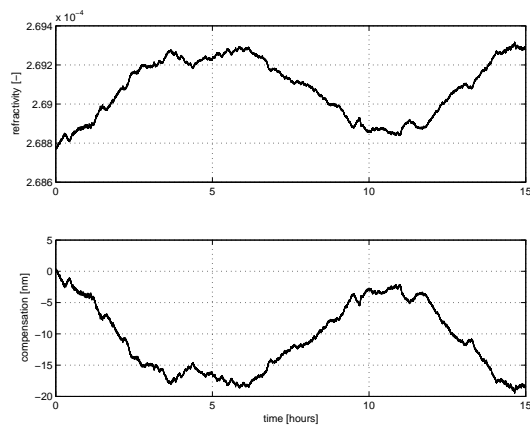
Figure 5.4: Top: measured refractivity. Bottom: calculated compensation [nm]

5.2.2 Results

The results are shown in figure 5.2 to 5.4.

5.2.3 Analysis

Changes in environmental conditions are seen in figure 5.2. This leads to a change in refractivity and a drift in the uncompensated laser signal 5.3. The compensation algorithm doesn't seem to improve this signal however: the drift even increases when the algorithm is used. The algorithm does however seem to accurately compensate for changes in the measured refractivity, looking at figure 5.4. When the refractivity increases, negative compensation is applied, as expected (see page 17). It indicates that other influences cause a drift in the laser signal.

Figure 5.5: Environmental changes during time
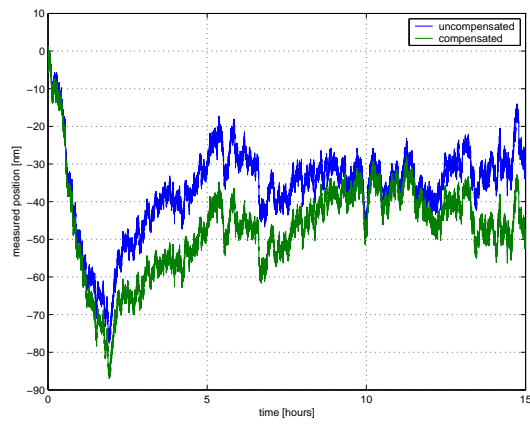

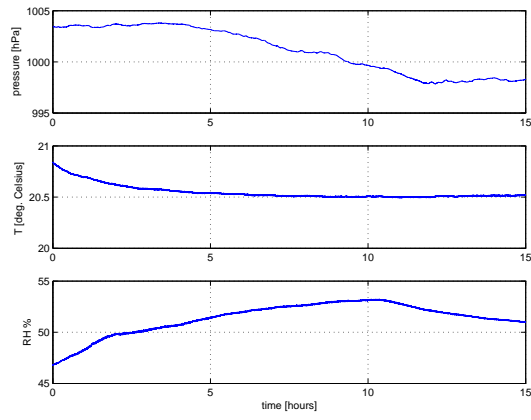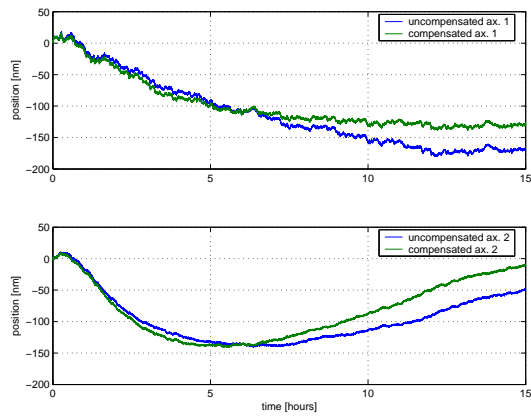Figure 5.6: Accumulated counts, converted to nanometers, measured with laser
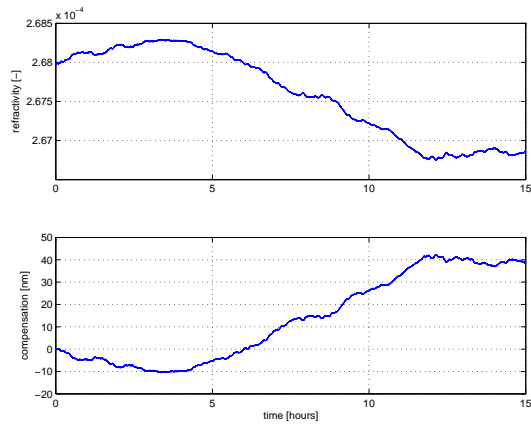
Figure 5.7: Top: refractivity. Bottom: calculated compensation [nm]

5.3 Influence turbulence

5.3.1 Description experiment

This experiment is done to find out if the drift in the previous experiment is caused by a movement of the stage. Furthermore the influence of airflow through the laser path is investigated. Therefore the measurement beam of the first axis is shielded by a small steel tube and stage two is disconnected from the motor by removing the pushrod of stage two.

5.3.2 Results

The results are shown in figure 5.5 to 5.7.

5.3.3 Analysis

Again there is no significant improvement due to compensation for a changing refractivity. Both axes show a drift of approximately 150 nm. The shielded measurement beam also does not improve the measurement. Axis two however does show a much smoother signal. This indicates that a stage which is connected to the motor performs small unwanted movements (with an amplitude of about 10 nm) relative to the interferometer, probably due to thermal gradients. It seems likely that thermal gradients in the structure are also causing large changes in the distance between the interferometer and the stages: the base plate length or shape changes. These thermal effects are larger than expected and need to be investigated more thorough.

Figure 5.8: Stages in original setup (top) are replaced by cube (bottom)
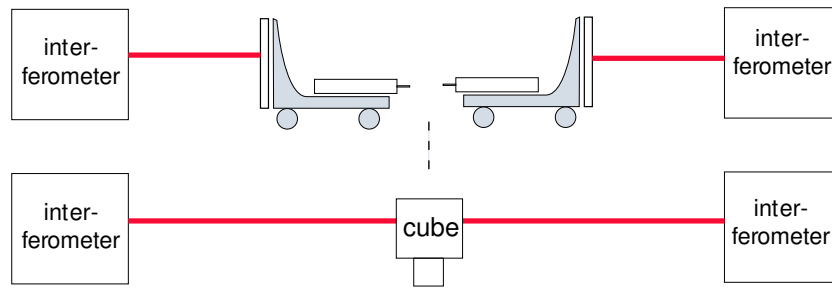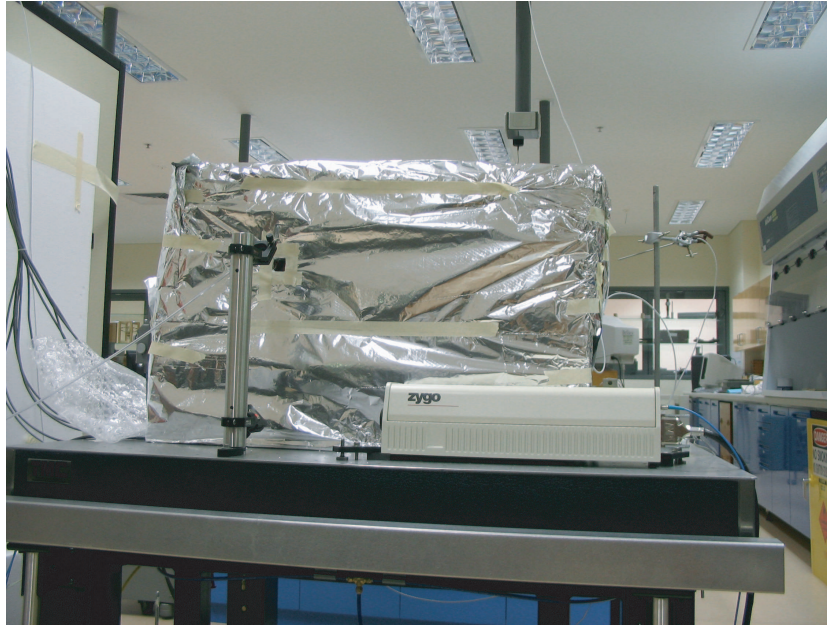

Figure 5.9: Photo of setup with box

5.4 Influence surroundings on structure

5.4.1 Description experiment

Goal of these experiments is to find out how the PCC structure is influenced by temperature changes. Both stages are removed and the cube gauge is placed in the center of the plate (see figure 5.8). The total dead path length is now about 220 mm. A drift in the compensated laser signal will now only occur if the baseplate or cube change in length.

Several PRT's are placed around the PCC structure and inside the measurement box to measure the air temperature at these locations. They show that the air temperature around and inside the PCC rises relative to the lab temperature. This was caused by several power sources in the vicinity of the structure. In the measurement box the sensors measured a $0.8°C$ rise due to the computer, a $0.4°C$ rise due to the laser and a $0.1°C$ rise due to the humidity sensor. The influence of the computer was canceled by moving it further away from the setup and placing it behind thick layers of polystyrene foam. The humidity sensor and the laser couldn't be moved.

A temporary solution was building a polystyrene box, covered with aluminium foil and bubble wrap, around the structure. This is to make sure the temperature inside the box is the same and rather constant after a certain amount of time. Figure 5.10 shows how the temperature in the box settles at about $0.8°C$ higher than lab temperature. At $t = 4$ hour the box is placed over the instrument. The temperature inside the box settles in about three days and is not influenced by rapid changes in lab temperature.To investigate the influence of a changing temperature on the structure, a measurement is done while the temperature in the box is still steadily increasing.
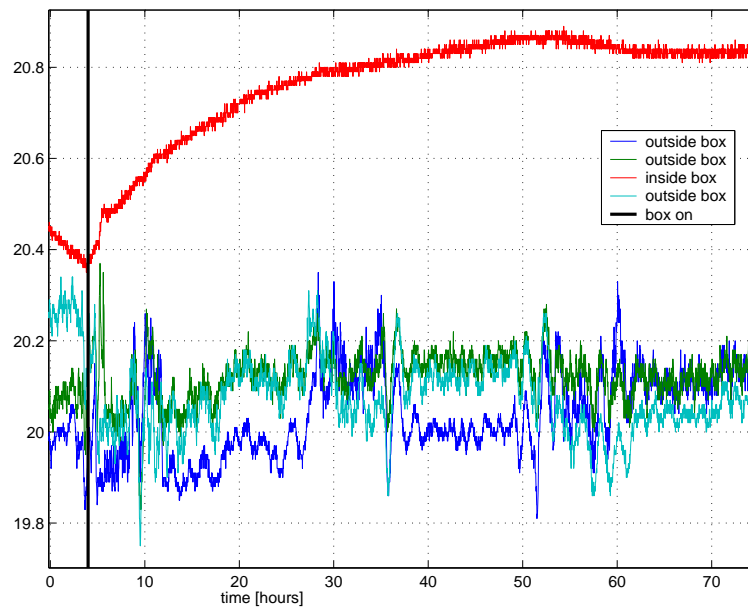
Figure 5.10: Temperature readings in time of four PRT's at different locations.

Figure 5.11: Environmental changes during time

Figure 5.12: Accumulated counts, converted to nanometers, measured with laser

Figure 5.13: Top: combined signal of both axes. Bottom: combined signal of both axis minus the calculated expansion of cube and plate.

5.4.2 Results

The results are shown in figure 5.11 to 5.13.

5.4.3 Analysis

As seen in figure 5.12, the algorithm compensates for changes due to a changing refractivity. If the signals of both axes are combined (top graph of figure 5.13), it is seen that the distance between the two interferometers has increased with 750 nm due to a temperature increase of $0.11°$C (or a drift of about 680 nm/mK). The thermal expansion of the cube (11.5ppm/$°$) and stainless steel plate (9.9 ppm/$°$) can now be subtracted (bottom graph of figure 5.13). After subtracting this estimated expansion there is still a residual drift of about 160 nm. This could mean that the stainless steel top plate is not only expanding but also bending.
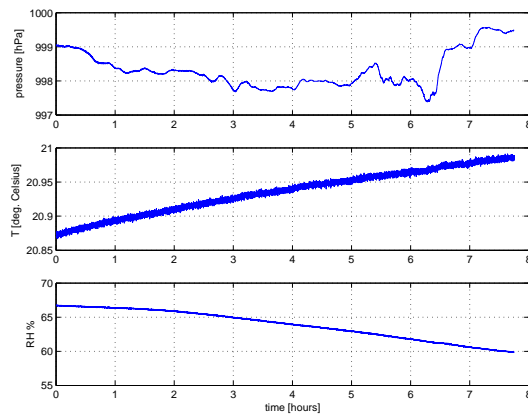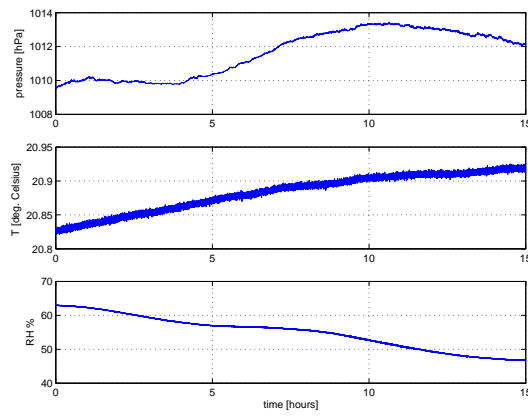
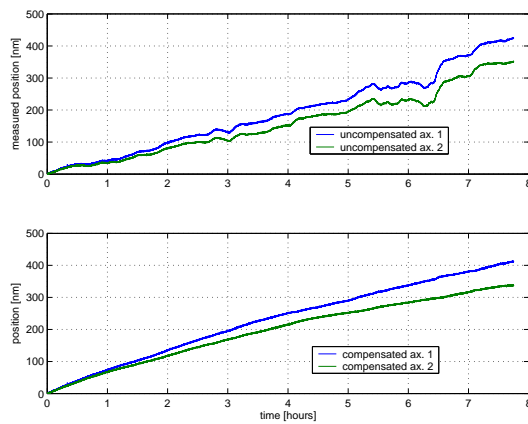Figure 5.14: Environmental changes during time

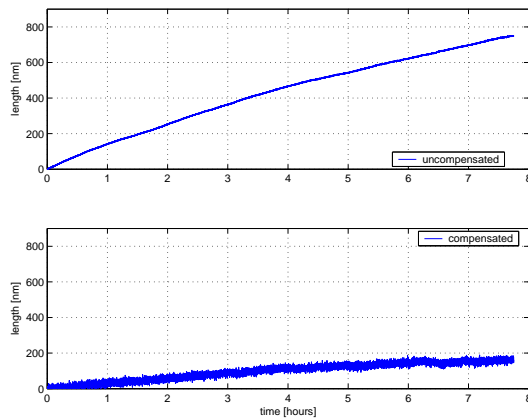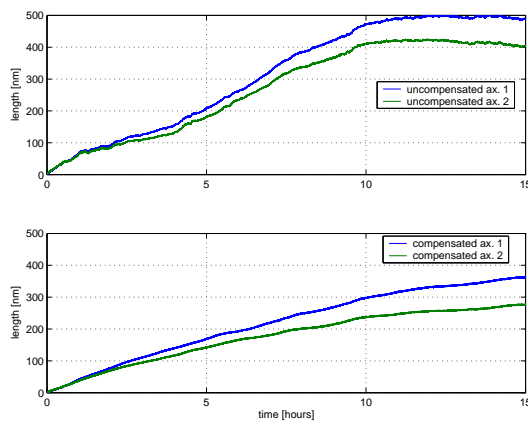Figure 5.15: Accumulated counts, converted to nanometers, measured with laser
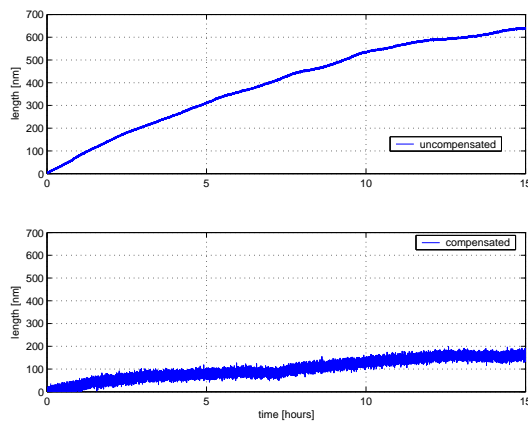
Figure 5.16: Top: combined signal of both axes. Bottom: combined signal of both axis minus the calculated expansion of cube and plate.

5.5   Bending structure

5.5.1   Description experiment

Goal of this experiment is to find out if there are temperature gradients in the structure in similar conditions as the previous experiment. These gradients could cause bending of the structure.
Ten thermistors are placed on the structure to monitor the temperature during an overnight measurement. The location of the thermistors is shown in figure 5.17. These thermistors are connected to the HP relay scanner. Connected to the scanner is a Scientific Hart thermistor read out.
LabVIEW software is written (see Appendix A) to communicate with the HP scanner and Scientific Hart device, both using an IEEE interface. LabVIEW scans through the thermistors, reads out the resistance and calculates the temperature based on calibration data (see Appendix B).

5.5.2   Results

The results are shown in figure 5.14 to 5.18.

5.5.3   Analysis

A drift of about 680 nm/mK is witnessed, which matches the previously obtained value. In figure 5.18 it is seen that temperature changes in the structure are not equal: relative temperature changes occur.
Thermistor number one shows the highest temperature, which can be explained since it is closest to the table and the laser. The metal table probably conducts heat from the laser into the structure. A new experiment is done to see if small temperature gradients can leed to bending of the structure.
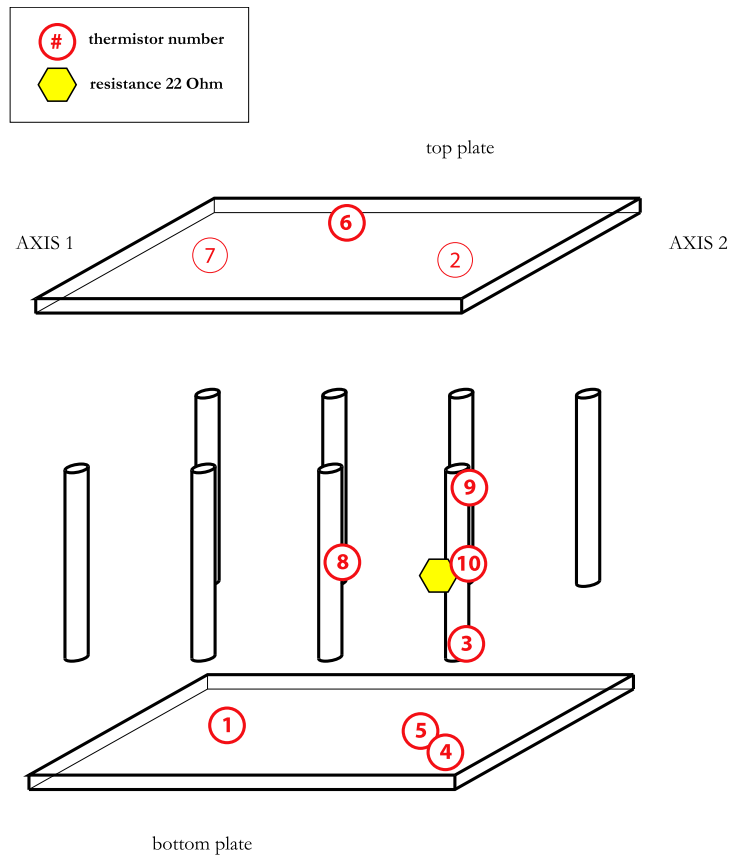
Figure 5.17: Location of thermistors. Location of resistance also shown, see paragraph 5.6
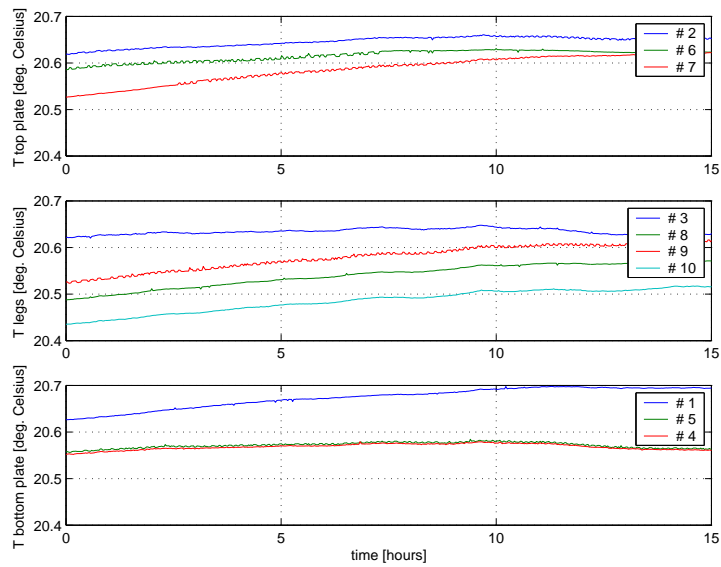
Figure 5.18: Temperature measured by thermistors.

5.6 Induced temperature gradient

5.6.1 Description experiment

A resistance of 22 Ohm is taped onto one of the legs of the structure, see figure 5.17. By controlling the current through the resistance, the temperature of the resistance can accurately be controlled. Goal is to see what the effect of an 50 mK temperature change is on the structure.

The measurement is done four days after placing the box over the instrument, when the temperature in the box has stabilized.

5.6.2 Results

The results are shown in figure 5.19. Shown are the drift measured by the laser and the temperature of locations in the vicinity of the resistance. Influence of the induced temperature rise was not witnessed in the readout of the other thermistors on the structure.

5.6.3 Analysis

It is seen that a 16 nm drift is witnessed when the temperature of one of the legs rises with 50 mK. After a short time delay, both ends of the leg also rise in temperature. Note that the resistance is positioned on one of the legs below axis two and axis one responds on the temperature input. This clearly shows that bending of the structure is a serious error source.
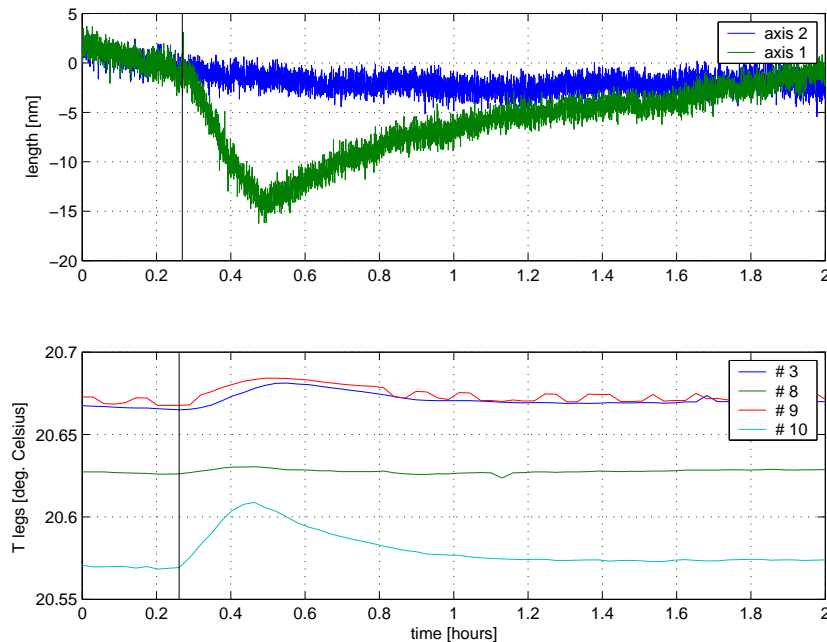
Figure 5.19: Top: accumulated counts, converted to nanometers, measured with laser. Bottom: temperature of the legs of the instrument, measured with thermistors. Heating up starts at black line at $t = 0.25$ and ends at $t = 0.46$ hours

5.7   Summary results

The algorithm implemented in a LabVIEW VI clearly compensates for changes in refractivity during the measurement. Shielding of the laser beam does not improve the measurement. Thermal changes influence the position of the stages and the length and shape of the top plate, therefore creating a significant error in the measurement process. An air temperature change of 0.1 K can result in a 600 nm error. Placing an insulating box over the instrument reduces the measurement uncertainties.

Chapter 6

Discussion

From the results we can conclude that the accuracy of the instrument is very temperature dependent. A 0.1 K air temperature change can result in a 600 nm error during a measurement and a temperature difference in the structure of only 50 mK can already cause a 17 nm error. Measuring a PCU with a maximum uncertainty of 10 nm would require a 1.6 mK stable environment. Since this is not possible with the present PCC setup, changes to the instrument are needed.

All external heat sources, like the laser and computer, should be placed as far away from the instrument as possible. Accurately monitoring the temperature of the instrument prior to any measurement is essential. A measurement should only start if the instrument is close to a thermal equilibrium. To achieve this equilibrium, a temperature controlled box should be placed over the whole structure. It will of course not be possible to create a controlled environment with deviations less then 2 mK. But even with a simple insulated box it was possible to reduce thermal gradients: during a two hour measurement the maximum drift was only 5 nanometer, see figure 5.19.

Bending of the top plate is a serious problem. It is mounted on eight legs and therefore statically overdetermined: any temperature change will result in internal stresses and complex bending shapes. The plate should be mounted in such a way that it is free to expand and shrink. This could be done by removing the bottom plate and legs and placing the top plate in a static determined way on the table. Mounting the PCU support upside down onto the top of the top plate would then be necessary. This could result in a smaller measurement loop when the probe makes contact with the PCU, since the current loop is very complex, see figure 6.1.
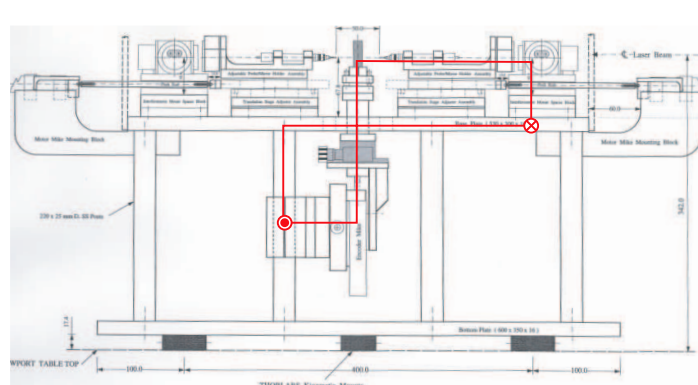
Figure 6.1: Measurement loop of axis 2

35
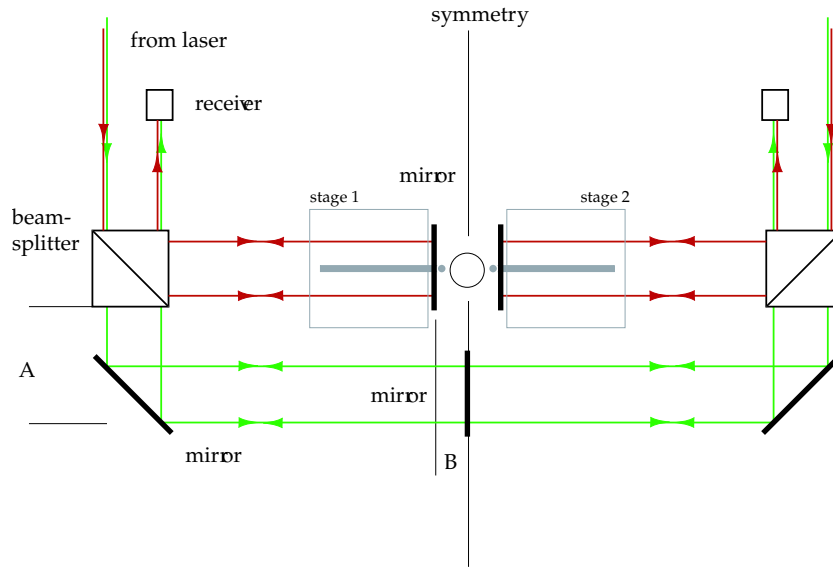
Figure 6.2: Top view of recommended optical configuration

New optical configuration

Errors due to pure expansion of the top plate can be minimized by replacing this part by a part
with a very low expansion coefficient. This is however expensive. An inexpensive solution is to
make the measurement setup insensitive for changes in the length of the top plate. In the cur-
rent setup, a measurement is done by measuring the displacement of the stages and assuming the
distance between the interferometers and distance between the target mirror and probe tip don't
change [1], see figure 6.3. Expansion of the top plate or stage will generate an optical path change
between the reference- and measurement beam and therefore a change in accumulated counts.
A new optical configuration is recommended for which a physical path change between interferom-
eter and target mirror will not cause an optical path change. This optical configuration is shown
in figure 6.2 [10].

In this configuration, both interferometers are capable of lateral movement without influencing
the count readout. We would not measure the distance between the interferometers, but between
the target mirrors as sketched in figure 6.4 (compare with figure 6.3). Furthermore the amount
of steel between target mirror and probe tip is drastically reduced.

---

[1]When the probe is at it's zero position.

Figure 6.3: Positionchanges A_1 and A_2 are measured, distance B_i and C are assumed not to change.
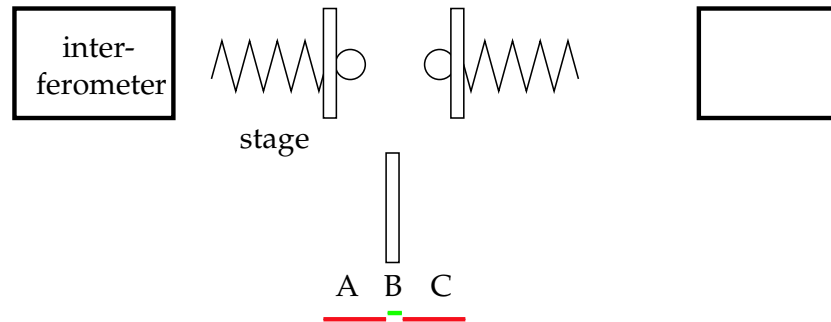
Figure 6.4: Measurement distance new setup. Measuring distance A and C, B is known.

The total deadpath distance, consisting of A and B (figure 6.2), can be minimized and be compensated for. To minimize deadpath distance B the targetmirror should be placed as close to the probe tip as possible. Suggestion is to drill a hole in the center of the targetmirror and place the tip through the mirror.

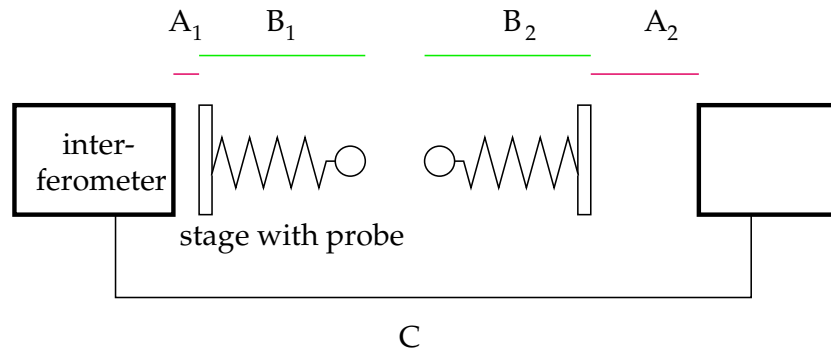The consequences of moving the targetmirror to the other side of the stage is investigated. The center of rotation of the stage is assumed to be halfway between the tip and probe. Pitching and yawing of the stage around this point will cause the center of the mirror and probe tip to describe a spherical path, see figure 6.5. A rotation of α would cause the probe tip to indicate a distance of x less, with

$$x = 2Rsin^2\left(\frac{\alpha}{2}\right),\tag{6.1}$$

and the mirror would move along the path of the virtual measurement beam with a distance y, with

$$y = \left(\frac{1}{cos(\alpha)} - 1\right)R.\tag{6.2}$$

It is assumed that the laser measures the position of the mirror spot on the virtual measurement beam. The error due to a rotation of α is, for the present setup $x - y$, for the mirror in the center of the stage x and for the mirror at the same location as the probe tip $x + y$. Yaw of 10 arcseconds is previously measured on the stage going through it's full range of motion. From figure figure 6.6 it can be concluded that moving the mirror to the front end of the stage has a negative effect on the accuracy and can result in an error of about 0.4 nm. However, an equal error would occur in the present setup if the steel between the targetmirror an the probetip would expand due to a temperature change of only 0.3 mK. Two other disadvantages should be considered when the target mirror is moved towards the probe tip. The cosine error due to misalignment
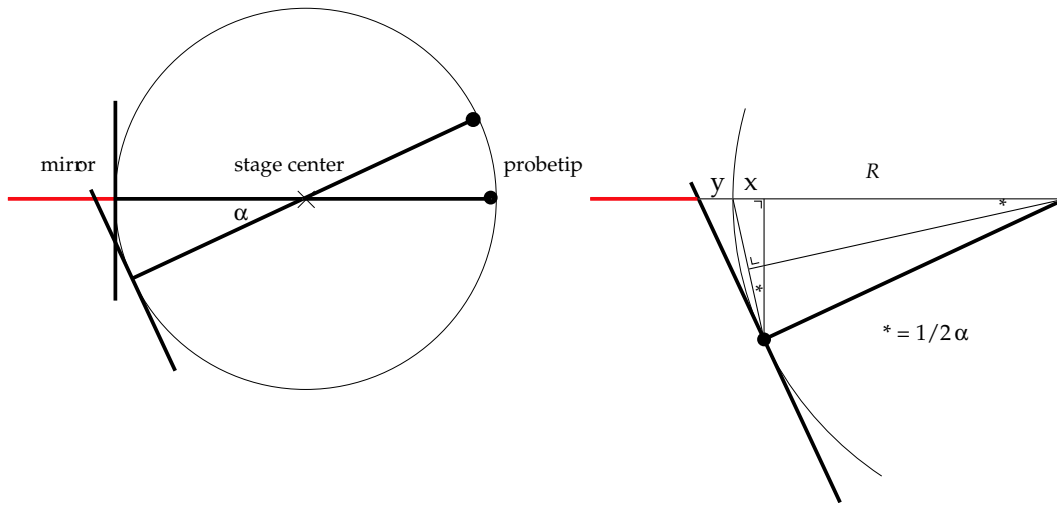
Figure 6.5: Left side: rotation around center of stage. Right side: close up of rotation. Tip and center of mirror lying on spherical path. The red line indicates the virtual measurement beam of the four pass interferometer.
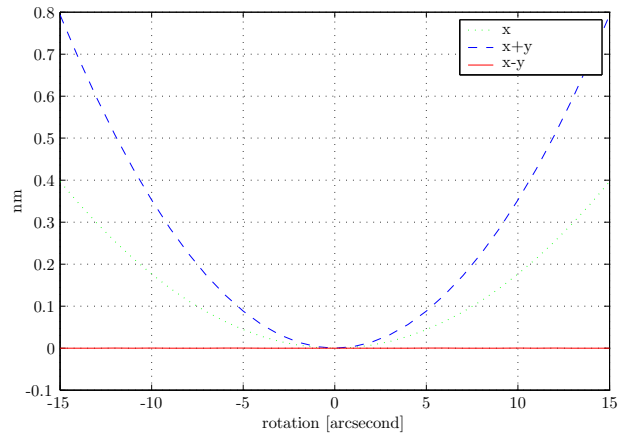
Figure 6.6: Error due to a rotation of the stage.

between the measurement laser beam and the axis of motion will increase. Furthermore a four pass interferometer is very sensitive to tilts of the target mirror. A small rotation of the mirror will cause the reflected beam to follow a different path than the incoming beam. After four passes this could mean that the measurement beam does not overlap the reference beam in a sufficient way. The use of retroreflectors instead of plain mirrors could resolve this problem but asks for a complete reconfiguration of the optical system. Attention should also be paid that measurement and reference beam should pass an equal amount of glass for thermal stability.

Chapter 7

Conclusion

Research has been done to determine large uncertainties when performing measurements with the Piston Cylinder Calibrator.

The influence of a changing refractive index of air during the measurement is examined. When monitoring temperature, pressure and relative humidity changes, changes in refractive index of air can be calculated and successfully compensated for while measuring.

The influence of temperature changes within the structure are examined. Several experiments are performed. Temperature gradients of only 0.1 K can cause uncertainties as large as 600 nm. Creating a thermal stable environment around the instrument is essential to minimize uncertainties caused by airflow and temperature gradients. Recommendations are done to minimize the influence of temperature changes on the measurement process.

LabVIEW software is written to perform measurements with the instrument using one software program. LabVIEW is used to operate and adjust control settings for the two DC motors which are part of the instrument. Research has been done to find a suitable PID controller for the motors in combination with the stages.

Appendix A

LabVIEW VI's

A.1   IEEE interface settings

The Windows IEEE interface settings shown in table A.1 have proven to successfully work in combination with the LabVIEW VI's.

IEEE setting	ZYGO Laser	HP scanner	Scientific Hart
Device Name	DEV1	DEV2	DEV3
Interface	GPIB0	GPIB0	GPIB0
Primary address	3	9	22
Secondary address	none	none	none
Send EOI	-	yes	-
Terminate read	yes	-	yes
Set EOI with EOS	yes	-	yes
8-bit EOS compare	-	-	-
EOS byte	10	0	10
Timeout I/O	1	1	1
Timeout Serial Poll	1	1	1
Readdress	yes	-	-

Table A.1: IEEE interface settings for the ZYGO Laser measurement board, the HP scanner and the Scientific Hart thermistor readout.

A.2   COM port settings

The COM port settings shown in table A.2 have proven to successfully work in combination with the LabVIEW VI's.

Port setting	SETRA	VAISALA
Port binding	COM3	COM2
Baud rate	2400	9600
Data bits	8	7
Parity	none	even
Stop bits	1	1
Flow control	none	none

Table A.2: COM port setting for the SETRA pressure sensor and VAISALA humidity sensor.

A.3   Communication with laser

To communicate with the ZMI 2001 measurement board, the low level *wput* and *lget* commands should be used [13]. These commands allow you to read and write to all the registers of the ZMI 2001 board. For example:

Turn on LED measurement board axis 1:

```
WPUT #H2D, #H1008, #H01
```

Turn off LED measurement board axis 1:

```
WPUT #H2D, #H1008, #H00
```

The $#H$ modifier is present to show that hexadecimal command lines are used. The $#H2D$ modifier is present to show that A16 addressing is used (A24 is also available not common). The board addresses of board 1 is set to 1000, board 2 to 2000. An offset from this address shows the register that is addressed.

To read the position information, the following commands can be used:

```
LGET? #H2D,#H1014
LGET? #H2D,#H2014
```

More information can be found in The ZYGO manual [13] command dictionary located in the Chassis and Control Board portion of the manual and the Measurement Board section. For a quick reference use pages, A2 and A3 of OMP0403 of the manual.

A.4   All LabVIEW VI's

A list of important LabVIEW VI's used during the research project. The names of these files are:

- PCC total.vi

- Ciddor.vi

- HPscanner.vi

- setra.vi

- vaisala.vi

- thermist.vi

- coeff.vi

- hart.vi

- counttonm

- compensate counttonm

- hexstring

- string

- zygomeasure

The relation between all VI's is shown in figure A.1. In the following paragraphs, a short description is given of all the VI's.
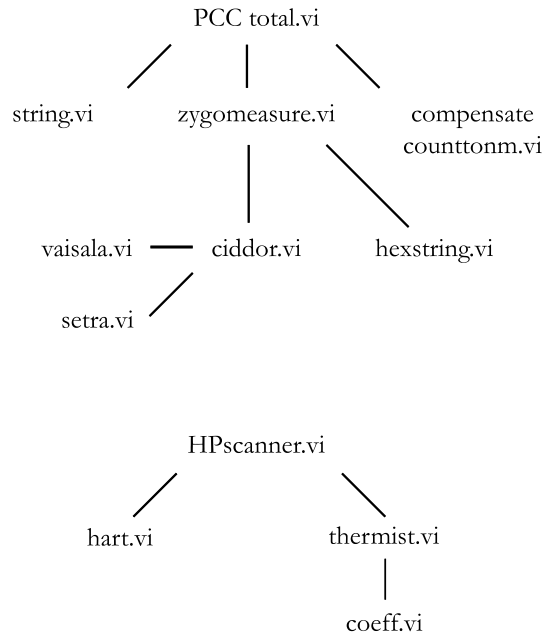

Figure A.1: Relation between all LabVIEW VI's.

A.4.1 PCC measurement VI's

PCC total.vi

Goal of this VI is to monitor and log all measured and calculated variables. It logs the sample number, counts of both axes, refractivity, relative humidity, pressure, temperature and the compensated amount of counts converted to nanometers.

The VI consists of 4 main sequences:

- 0. measurement can start at a certain date and time (optional)

- 1. check laser for errors and report what the error number and description is

- 2. initialize the vaisala sensor
  wait
  calculate the refractive index of air at t=0 to use in compensation algorithm
  reset both measurement boards (set count to zero)

- 3. use *zygomeasure.vi*and *compensate couttonnm* to retrieve all data

Note that the maximum sample frequency of this VI is 3 Hz due to slow COM port communications. Not using any COM port connections, the sample frequency can be 200 Hz.

Zygomeasure.vi

Main goal of this VI is to retrieve count data form the ZMI 2000 measurement board for both axes at a variable sample rate. It uses the VI's *vaisala, setra, ciddor* and *hexstring* to retrieve the actual temperature, relative humidity and pressure and calculate the refractive index of air. Error messages windows will pop up if communication with the setra sensor, vaisala sensor or interferometer fails.

The VI consists of 8 sequences:

- 0. send a request to measurement board no. 1 to latch a position signal

- 1. send a request to measurement board no. 1 to latch a position signal

- 2. receive position signal axis 1

- 3. receive position signal axis 2

- 4. retrieve environmental variables or uses standard values
  calculate refractive index of air

- 5. hexadecimal output of board 1 is converted to a decimal value

- 6. hexadecimal output of board 2 is converted to a decimal value

- 7. wait for a variabale amount of seconds

Hexstring.vi

Output of the laser is a 32 bit hexadecimal value, which represents a 32 bit 2's complements word. That means at the transition from zero to negative, all bits switch to logic 1. The addition $\#H$ is removed.

String.vi

Sends any command line to the ZMI 2000 measurement boards. Reading output from the boards is optional.

Counttonm.vi

Converts counts to nanometers, without compensating for the deadpath length. Refractivity changes will influence measurement. Preferably use VI *Compensate counttonm.*

Compensate counttonm.vi

Converts counts to nanometers and compensates for the deadpath length.

Ciddor.vi

Goal is to calculate the refractive index of air and refractivity for any given wavelength of light, temperature, pressure, relative humidity and CO_2 content.

Vaisala.vi

Goal of this VI is to read-out the Vaisala humidity sensor for a temperature and relative humidity reading. The Vaisala sensor can do a single or continues measurement. It was found that LabVIEW can have trouble reading the sensor output. Using the single measurement, LabVIEW sometimes suddenly reads the character > which stops the measurement. This is not the case for continues readings, so this option is preferred. Windows Hyperterminal is much faster in communicating with the sensor. This program is used to change the baud rate to 9600 and change the output of the sensor using the following command lines:

```
>FORM \<cr>
```

```
FORM <cr>
"xxx.xxx"
?\UUU.UUU\\t\TTT.TTT\\r\n
```

The temperature and relative humidity values are extracted from the output string.

Setra.vi

Using a simple print command *P* the pressure is read form the Setra sensor. The pressure value is extracted from the output string.

A.4.2 Thermistor

The LabVIEW VI used to measure the temperature using ten thermistors is not integrated into the main measurement VI: *PCC total*. The main reason is that the sample frequency of this VI very different: 0.25 Hz.

Hpscanner.vi

Goal of this VI is to monitor the temperature of ten thermistors in time and log this data into a spreadsheet. The VI consists of 4 sequences:

- 0. measurement can start at a certain date and time (optional)

- 1. after a reset of the HP 3488A scanner, channel 00 of board number 2 is closed to supply current to relay board of the scanner.

- 2. wait 2 seconds to close channel

- 3. scan channels 0 to 9 of board 1
  use *hart.vi* to measure resistance of thermistors number 1 to 10
  convert resistance to temperature for each thermistor using *thermist.vi* log data in a spreadsheet and show data in a graph

Thermist.vi

Goal is to convert the resistance measured with the Scientific Hart thermistor read-out to temperature in degrees Celsius using the thermistor coefficients stored in *coeff.vi*.

Hart.vi

Goal is to retrieve the measured resistance with the Scientific Hart thermistor read-out.

Appendix B

Thermistor calibration

B.1 Calibration data

The thermistors used were calibrated in 2003. The thermistors are submerged in an oil bath and the resistance is measured for different bath temperatures.

In the experiments performed in this research project, resistance is measured and needs to be converted to degrees Celsius using the Steinhart-Hart equations [2]. The equation is derived from mathematical curve-fitting techniques and examination of the resistance versus temperature characteristic of thermistor devices. In particular, using the plot of the natural log of resistance value, $ln(R)$ versus $(1/T)$ for a thermistor component to consider $(1/T)$ to be a polynomial in $ln(R)$, an equation of the following form is developed:

$$T = \frac{1}{C_1 + C_2 * ln(R) + C_3 * ln(R)^2 + C_4 * ln(R)^3} \tag{B.1}$$

Four resistances per thermistor at different temperatures are needed to find the four constants C_1 to C_4. Matlab is used to solve these four equations. The following constants are found.

Constant	Thermistor 1	Thermistor 2	Thermistor 3	Thermistor 4	Thermistor 5
C_1	$-1.65 \cdot 10^{-1}$	$-1.34 \cdot 10^{-1}$	$1.23 \cdot 10^{-1}$	$9.92 \cdot 10^{-2}$	$-1.28 \cdot 10^{-1}$
C_2	$5.31 \cdot 10^{-2}$	$4.34 \cdot 10^{-2}$	$-3.86 \cdot 10^{-2}$	$-3.11 \cdot 10^{-2}$	$4.12 \cdot 10^{-2}$
C_3	$-5.62 \cdot 10^{-3}$	$-4.58 \cdot 10^{-3}$	$4.13 \cdot 10^{-3}$	$3.33 \cdot 10^{-3}$	$-4.35 \cdot 10^{-3}$
C_4	$1.99 \cdot 10^{-4}$	$1.62 \cdot 10^{-4}$	$-1.46 \cdot 10^{-4}$	$-1.18 \cdot 10^{-4}$	$1.54 \cdot 10^{-4}$
Constant	Thermistor 6	Thermistor 7	Thermistor 8	Thermistor 9	Thermistor 10
C_1	$-1.12 \cdot 10^{-1}$	$-1.08 \cdot 10^{-1}$	$1.58 \cdot 10^{-1}$	$2.91 \cdot 10^{-1}$	$3.26 \cdot 10^{-1}$
C_2	$3.63 \cdot 10^{-2}$	$3.50 \cdot 10^{-2}$	$-4.98 \cdot 10^{-2}$	$-9.23 \cdot 10^{-2}$	$-1.03 \cdot 10^{-1}$
C_3	$-3.83 \cdot 10^{-3}$	$-3.69 \cdot 10^{-3}$	$5.31 \cdot 10^{-3}$	$9.83 \cdot 10^{-3}$	$1.10 \cdot 10^{-2}$
C_4	$1.35 \cdot 10^{-4}$	$1.31 \cdot 10^{-4}$	$-1.88 \cdot 10^{-4}$	$-3.48 \cdot 10^{-4}$	$-3.90 \cdot 10^{-4}$

Table B.1: Calculated thermistor coefficients

Bibliography

[1] March 2005. `http://www.pmdcorp.com/support/manual/1401_manual.pdf`.

[2] March 2005. `http://www.betatherm.com/stein.htm`.

[3] Norman Bobroff. Recent advances in displacement measuring interferometry. Technical report, 1993.

[4] P.E Ciddor. Refractive index of air: new eqautions for the visible and near infrared. Technical report, 20 March 1996.

[5] National Instruments Corporation. Labview version 6.0, 2000.

[6] Suzanne J.A.G Cosijns. *Displacement laser interferometry with sub-nanometer uncertainty.* Phd report, University of Technology, Eindhoven, 2004.

[7] J.E. Decker K. Bustraan S. de Bonth J.R. Pekelsky. Updates to the nrc gauge block interferometer. Nrc document no. 42753, National Reasearch Counsil Canada, Ottawa Canada, 2000.

[8] J. David Powell Gene F. Franklin. *Feedback control of dynamic systems.* Addison Wesley Publishing Company, 1994.

[9] Dr. J.R. Miles. Proposal for a new instrument for the measurement of diameter and form of cylinders. Internal report csiro, National Measuremnt Labaratory, Melbourne Branch, CSIRO, 1997.

[10] February 2005 Personal conversation with Dr. Nick Brown, NMI Clayton.

[11] G.E. Sommargren. A new laser measurement system for precision metrology. Technical Report 4, october 1987.

[12] C. R. Steinmetz. Sub-micron position measurement and control on precision machine tools with laser interferometry. Technical Report 1, january 1990.

[13] Zygo Corporation. *ZMI 2000 VME-PCI System Manual*, 2001.